A Global and Seasonal Perspective of Martian Water Vapor from ExoMars/NOMAD

Journal Item

A Global and Seasonal Perspective of Martian Water Vapor From ExoMars/NOMAD

M. M. J. Crismani[1,2], **G. L. Villanueva[3]**, **G. Liuzzi[3,4]**, **M. D. Smith[3]**, **E. W. Knutsen[3,4]**, **F. Daerden[5]**, **L. Neary[5]**, **M. J. Mumma[3]**, **S. Aoki[5,6]**, **L. Trompet[5]**, **I. R. Thomas[5]**, **B. Ristic[5]**, **G. Bellucci[7]**, **A. Piccialli[5]**, **S. Robert[5,8]**, **A. Mahieux[5]**, **J.-J. Lopez Moreno[9]**, **G. Sindoni[10]**, **M. Giuranna[7]**, **M. R. Patel[11,12]**, and **A. C. Vandaele[5]**

[1]Planetary Systems Laboratory, NPP/USRA, NASA Goddard Space Flight Center, Greenbelt, MD, USA, [2]Department of Physics, California State University, San Bernardino, San Bernardino, CA, USA, [3]Planetary Systems Laboratory, NASA Goddard Space Flight Center, Greenbelt, MD, USA, [4]Department of Physics, College of Arts and Sciences, American University, Washington, DC, USA, [5]Royal Belgian Institute for Space Aeronomy, Brussels, Belgium, [6]LPAP, STAR Institute, Université de Liège, Liège, Belgium, [7]Istituto di Astrofisica e Planetologia Spaziali, Rome, Italy, [8]Institute of Condensed Matter and Nanosciences, Université catholique de Louvain, Louvain-la-Neuve, Belgium, [9]Instituto de Astrofisica de Andalucía, Granada, Spain, [10]Agenzia Spaziale Italiana (ASI), Rome, Italy, [11]School of Physical Sciences, The Open University, Milton Keynes, UK, [12]Space Science and Technology Department, Science and Technology Facilities Council, Rutherford Appleton Laboratory, Oxfordshire, UK

Abstract Slightly less than a Martian Year of nominal science (March 2018–January 2020) with the ExoMars Trace Gas Orbiter has furthered the ongoing investigation of dayside water vapor column abundance. These dayside observations span latitudes between 75°S and 75°N, and all longitudes, which can provide global snapshots of the total water column abundances. In addition to tracking the seasonal transport of water vapor between poles, geographic enhancements are noted, particularly in the southern hemisphere, both in Hellas Basin, and in other regions not obviously correlated to topography. We report consistent water vapor climatology with previous spacecraft observations, however, note a difference in total water vapor content is noted. Finally, we are unable to find evidence for substantial diurnal variation in the total dayside water vapor column.

Plain Language Summary This work provides the first look at the ExoMars Trace Gas Orbiter's ability to track atmospheric water vapor on the day side of Mars, through downward looking observations. Water vapor is reported in a series of maps, with respect to geography and season, and find consistent water vapor climatology with precious spacecraft observations. These maps inform our understanding of where Martian water vapor moves throughout the year and where it is concentrated.

1. Introduction

Since the discovery of water vapor on Mars (Spinrad et al., 1963), the study of water in all of its forms (i.e., vapor, ice clouds, surface ices, and possibly brines) has been a primary science topic. Water vapor was established to behave in a similar fashion between Martian Years (MYs; Jakosky & Farmer, 1982), driven by significant seasonal exchange between the atmosphere, surface ice, and possibly directly with the regolith, although the impact of this exchange has not yet be definitively determined. However, there is an outstanding set of issues related to the potentially unbalanced transport of water between such reservoirs; whether there are major sources and sinks in the water cycle and if current models have identified the relevant processes for Martian seasonal transport (Montmessin et al., 2017). Many decades of observation have developed a rich understanding of atmospheric water climatology from the Mars Global Surveyor (MGS) Thermal Emission Spectrometer (TES; Smith, 2002, 2004), seasonal ice frosts from the Viking Infrared Thermal Mapper (Kieffer et al., 1976), ice-rich regolith from the Mars Odyssey Gamma Ray Spectrometer (Boynton, 2002), and others (Langevin et al., 2007; Smith et al., 2009). The north polar cap, an extensive permanent cap of CO_2 and H_2O ices, plays the most substantial role amongst surface reservoirs, injecting more than 10^{12} kg of water into the atmosphere every northern spring and summer (for a detailed review, see Montmessin et al., 2017).

Beginning with the Viking Orbiter Mars Atmospheric Water Detectors (MAWD; Jakosky & Farmer, 1982), to the MGS TES (Christensen et al., 2001), Mars Express' (MEx) Visible and Infrared Mineralogical Mapping Spectrometer (OMEGA; Bibring et al., 2006), Planetary Fourier Spectrometer (PFS; Formisano et al., 2005), and the Ultraviolet and Infrared Atmospheric Spectrometer (SPICAM; Bertaux et al., 2006) instrument suites, and the Mars Reconnaissance Orbiter (MRO) Compact Reconnaissance Imaging Spectrometer for Mars (CRISM; Murchie et al., 2007), water vapor has been observed in many orbital configurations and by probing differing wavelength regions. The wavelength regions where Martian water have been observed, from shorter to longer wavelengths include: SPICAM and MAWD at 1.38 μm, OMEGA, PFS-SW, CRISM at 2.56 μm, PFS-LW at 30 μm, and TES at 28–42 μm. While OMEGA, PFS-SW, and CRISM are most easily intercompared, TES provides one of the longest sets of continuous measurements, however, comparisons between this instrument and others come with the caveat that they measure different bands of water, and therefore, make different assumptions about modeling the absorption features, aerosols and surface at their respective wavelengths. Comparisons between these instruments shifted the original MAWD and TES reported water vapor columns to a lower value than initially reported (Fedorova et al., 2004, 2010; Fouchet et al., 2007; Pankine et al., 2010), however, most of the climatological features were similar between them. Previous works (e.g., Maltagliati, Montmessin, et al., 2011) have noted that the main features of the Martian water cycle are captured by all of these instruments, and the lack of agreement in peak values, during northern summer maximum for example, is a discrepancy that is not readily explained, nor within the uncertainties provided by the various retrieval methods.

In this work, we present water vapor retrievals from observations obtained with the Nadir and Occultation for MArs Discovery (NOMAD; Vandaele et al., 2018) instrument, part of the remote sensing instrument suite of the ExoMars Trace Gas Orbiter (TGO). The measurements sample dayside longitudes between 75°S and 75°N latitude range. In addition to tracking the seasonal transport of water vapor between poles, geographic enhancements are noted, particularly in the southern hemisphere, both in Hellas Basin, and in other regions not obviously correlated to topography. A comprehensive analysis of water vapor in the Martian atmosphere should consider its three-dimensional structure, photochemical pathways, and ice-cloud formation. Ozone is linked to water vapor through photochemical dissociation and photolysis, where their abundances are anti-correlated (Barth et al., 1973) and water-ice clouds are ubiquitous at Mars (Clancy et al., 2017). The observations included here contribute to one section of this puzzle, but future work will be necessary to address these three components together.

2. TGO/NOMAD Limb and Nadir Observatory (LNO)

Investigating how the water and geochemical environment varies by characterizing their distributions in the atmosphere is a primary goal of TGO, whose solar occultation (SO) instrument suite provides unprecedented coverage of Mars' atmosphere and further enhancing our understanding of the processes that control the loss of water from the surface and atmosphere. Unlike many of its Sun synchronous orbiting predecessors, TGO's 2-hr precessing orbit observes the day and nightside of Mars at many local times and latitudes. Remote sensing of the Martian atmosphere permits observations from the near planetary boundary layer to the thermosphere, at all latitudes and longitudes, and over all seasons in a Mars Year. The TGO/NOMAD instrument observes the Martian atmosphere in SO, limb, and nadir geometries.

Since the nominal science period began in March 2018, NOMAD has conducted a spectroscopic survey of Mars' atmosphere in UV, visible and IR wavelengths covering the 0.2–0.65 and 2.3–4.3 μm spectral ranges. NOMAD is composed of three channels (Neefs et al., 2015): a SO only channel operating in the infrared wavelength domain (Thomas et al., 2016), a second infrared channel capable of doing nadir and limb observations (LNO), and an ultraviolet/visible channel (UVIS) that can work in all observation modes (Patel et al., 2017). The SO and LNO channels are an updated and improved versions of SOIR from the Venus Express (Vandaele et al., 2013), and UVIS is based on the design from the Humboldt ExoMars lander. NOMAD offers an integrated instrument combination of a flight-proven concept that provides mapping and vertical profile information at high spatio-temporal resolution.

2.1. Instrument Calibration and Data Processing

The LNO channel has its own optical baseplate, but shares the same single interface to the spacecraft as the SO and UVIS channels. The LNO detector is an actively cooled HgCdTe Focal Plane Array. The optical layout of LNO is identical to that of SO using an echelle grating with a groove density of 4 lines/mm in a Littrow configuration in combination with an Acousto-Optic Tunable Filter (AOTF) for spectral window selection. The width of the selected spectral windows varies from 20 to 35 cm^{-1} dependent on the selected diffraction order. The LNO channel measures in the wavelength range between 2.3 and 3.8 μm, with a typical resolving power ($\lambda/\delta\lambda$) in the 10,000–15,000 range. For orders 167–169 (2.61–2.66 μm) used here, the effective resolving power of the instrument was found to be 10,500.

Spectral frequency and AOTF calibration were treated according to the formalism and the results in Liuzzi et al. (2019). The frequency calibration of LNO takes into account temperature fluctuations and is derived with an accuracy of 0.1 cm^{-1}. The AOTF functional form was slightly adapted from the one derived for SO, where the AOTF is described by the sum of a sinc squared function and a baseline, and the use of a multiplicative factor for the sinc sidelobes amplitude. Based on in-flight calibration of the spectra considered in this study, the LNO AOTF response function is described by a simple sinc squared function with a main lobe of width 22 cm^{-1} and no baseline. Instrument temperature fluctuations are found to affect the central position of the AOTF on the detector, however, this shift was found to be regular (0.25 cm^{-1} K^{-1}) and thus accounted for. The AOTF shift with temperature has been estimated directly from the LNO measurements, by minimizing spectral residuals as a function of AOTF center on a subset of spectra acquired in different illumination conditions and regions, thus inferring the dependency of AOTF position on AOTF frequency and temperature. This preliminary calibration is important because shifts in the AOTF center frequency caused by temperature have the effect of modifying the relative contribution of the central (observed) diffraction order with respect to nearby orders. This results in a variation of the observed depth of water lines that can be as large as 10%, and is considered in the overall systematic uncertainty of the retrieval. The primary sources of stochastic noise in the instrument are the thermal background due to the instrument temperature (particularly high for the LNO channel due to thermal dissipation; standard for this form of detector) and digitization error, which is significant particularly in the LNO channel of NOMAD, since counts are low compared to the thermal background signal. Once the background is subtracted, this source of noise is the result of quantization that can cause measured values to fluctuate between different quantization levels (Griffiths & Haseth, 2007). To account for low signal and/or high noise data, the data products considered herein have been filtered by solar zenith angle (SZA) < 60°, such that a SNR of >1 is ensured for the continuum. A composite error is then assigned to the data prior to the retrieval process, constructed large enough to represent the root mean square deviation of the data during the orbit.

This analysis used the level 0.3a NOMAD LNO data (described at https://nomad.aeronomie.be), with spectra expressed in detector counts. Following the principles successfully used with previous Nadir observatories for example (Smith et al., 2009), these observations are radiometrically calibrated using dedicated LNO calibration observations, where the instrument is pointed toward the Sun. Using the known solar flux (Hase et al., 2010) an instrument throughput is derived for every order, establishing a correspondence between the number of counts in LNO observations and radiance as a function of wavelength (order) as well as the various observational and geometrical parameters. This relation is used to convert counts to a flux ratio (I/F)—for Nadir observations is equivalent to a reflectance factor. In detail, the I/F is constructed by considering instrument exposure time (t_{exp} [s]), number of integrations (n_{exp}), collecting area (A_{tele} [m^2]), wavelength dependent solid angle (Ω [sr]), spectral pixel width ($\delta\lambda$ [μm]), and the source spectral radiance (L [W sr^{-1} m^{-2} μm^{-1}]), where the integrated flux (either I or F) is constructed as:

$$I \text{ or } F = L_{I \text{ or } F} \, t_{exp} \, n_{exp} \, A_{tele} \Omega \, \delta\lambda \, \lambda \, 1e^{-6}/hc$$

For both I and F, the spectral radiance L naturally encompasses the contribution from the main order and the nearby orders due to the AOTF filtering, therefore the calculated I/F will naturally include the contribution from the nearby orders. Since this work considers only orders 167–169, which are dominated by solar reflected sunlight, and does not compare to others far from this spectral interval, radiometric calibration of the instrument is less important than the I/F data product, where the temperature-independent component of the instrument response function is modeled out by the F reference itself. As said, the AOTF convolves
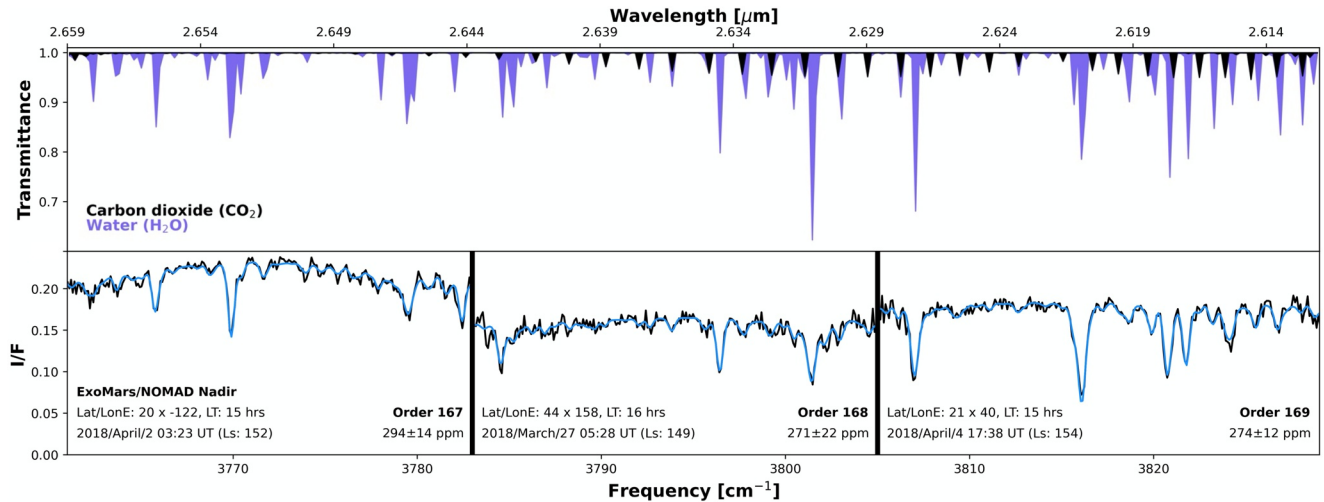
Figure 1. Top: a simulated spectrum of CO_2 (black) and H_2O (purple) showing the relative line depth and locations, without the presence of atmospheric aerosols, surface albedo, or geometric absorption. Bottom: Trace Gas Orbiter's Nadir and Occultation for MArs Discovery/limb and Nadir observatory observed spectra (black) obtained in nadir geometry and compared to a best fit model (blue). These data consist of three adjacent orders (167, 168, and 169) separated by a black vertical line and are representative of similar retrieved water content, shown in the bottom right of each inset.

low level contribution from nearby orders, and this is modeled by the AOTF side lobe function for this narrow spectral region (see details in Liuzzi et al., 2019). The albedo of the Martian surface does not have sharp spectral variations across a few spectral orders, and acts to raise or lower the overall flux. Using I/F is less sensitive to these differences and thermal emissions is negligible at the wavelengths considered (i.e., solar reflected planetary fluxes), therefore water vapor retrievals are mainly dependent on the intensity of the narrow molecular absorptions in I/F spectrum. However, these retrievals are dependent on the assumed temperature profile impacting the partition functions and relative intensity of the lines. We have tried to minimize/mitigate this effect by using parameterized climatological data (see details below).

Despite the solar zenith angle constraint on LNO observations of the dayside of Mars (SZA < 60°), this still allows for a variety of sampled geophysical conditions. This data set samples local times from 8 to 16 hr, latitudes from 75°S to 75°N, and all longitudes. As the orbit of the spacecraft goes from one terminator in the north to the opposite in the south (e.g., dusk to dawn), the LNO channel maps out slices across the surface. Because the orbit of TGO slowly precesses, to cover northern and southern latitudes on both dawn and dusk terminators, this invariably mixes observations of local time and latitude with season.

3. Water Vapor Retrievals

Absorption by H_2O is a dominant feature in nadir observations in the selected diffraction orders (Figure 1), and is reliably retrieved in all dayside profiles where the SZA is less than 60°. The three diffraction orders predominantly used to retrieve water are orders 167, 168, and 169 (3,754–3,829 cm^{-1}; Figure 1). These orders were selected as they include H_2O absorption lines (ν_3, vibrational band) that are optically thick enough to be always detectable; nevertheless, there are additional orders that may, with future data processing, yield retrievals of H_2O, HDO, CO_2, or CO.

Atmospheric water vapor is retrieved with a state-of-the-art radiative transfer suite, the Planetary Spectrum Generator (PSG), which models absorption features of water vapor, as well as absorption and scattering of ambient gases and aerosols with the Planetary and Universal Model of Atmospheric Scattering (PU-MAS; Villanueva et al., 2018). Atmospheric emission, scattering and absorption is modeled layer-by-layer along the line of sight for a variety of observing geometries, where full three-dimensional calculations are performed (Smith et al., 2013). A global map of the surface albedo of Mars is derived from the CRISM Mars Reduced Data Records reflectance products (Murchie et al., 2007), and interpolated to be appropriate for the spatial resolution of TGO. The retrieval process used in PSG is based on an Optimal Estimation (OE) approach (Rodgers, 2000); details on how this is implemented in PSG to treat TGO data are found in

previous work (Liuzzi et al., 2019), although in this case the same fundamental OE equations are used to treat Nadir data and derive total columns rather than vertical profiles. Water vapor retrievals utilize a priori atmospheric information from climatological databases such as the Mars Climate Database (MCD; Millour et al., 2015) or global circulation models such as the Global Environmental Multiscale model (GEM; Neary & Daerden, 2018). While retrievals are impacted by the assumed climatological state (i.e., partition function and relative intensity of lines), numerical experiments between GEM and MCD a priori atmospheric states led to retrieved differences ~10%, which is within the systematic error assigned for these water retrievals. This investigation employs the GEM climatological state, which includes a parameterization of the aerosols state during the time of the observations. Column integrated retrievals of optically thin species are mostly independent of the assumptions of their vertical distribution where a priori temperature-pressure profiles are not the determining cause for retrieved column abundance, with the exception of high aerosol opacities, which substantially limit the gas column accessible to Nadir observations.

Lofted dust and water ice clouds are a constant feature of the Martian atmosphere (see reviews from Clancy et al., 2017 for clouds and Kahre et al., 2017 for dust), however, initial studies with the LNO instrument broadband spectral analysis were not able to reliably distinguish between aerosol opacity along the nadir line of sight and surface albedo features and their variations. To address this, a study was performed on the effect of surface pressure and aerosol content on the broadband absorption spectrum at a variety of solar zenith angles using the scattering models of PSG/PUMAS. This demonstrated that dust is the dominant source of systematic uncertainty in the retrieved water column values, whereas water ice clouds must be in excess of 50 times their normal concentrations to significantly affect the retrieved abundances (which may be applicable to periods such as the Aphelion Cloud Belt season). While the surface pressure is taken into account in determining the water column from every spectrum, this cannot be straightforwardly done for profiles with high aerosol content (such as those found during the Global Dust Storm of 2018) and variable vertical distribution, because the information about the vertical profiles of aerosols relative to the observed water column cannot be reliably inferred by the limited set of diffraction orders used in this work. Therefore, definitive statements can only be made about the presence of water, not its absence. The presence of strong dust or water ice layers, forming a dust or aerosol top, can fully obscure the water vapor below these altitudes, and therefore these retrievals represent a lower limit to the total column.

Using OE (Liuzzi et al., 2016; Rodgers, 2000), each spectrum is individually analyzed to retrieve CO_2 and H_2O columns. The CO_2 column is retrieved as a scaling factor of the CO_2 profile itself, while keeping the temperature profile fixed to the a priori value provided by GEM (Neary & Daerden, 2018). The H_2O column, instead, is retrieved in terms of parts per million (ppmv), assuming a uniform vertical mixing ratio from the surface to the top of the atmosphere. A significant portion of the total water vapor column corresponds to the water vapor content of the first few kilometers above the surface, regardless of its vertical distribution, where the vertical profile shape was investigated in our retrievals with various a priori models and whose impact is included in the systematic uncertainty calculation. In addition, we have verified that the posterior Degrees Of Freedom (DOF) calculated with the classical OE approach is usually close to 1, meaning that no information is available beyond the water column itself. For water vapor retrievals, an a priori value of 50 ppmv is used, with an a priori variance of 100 ppmv, which encompasses the large variability that can be expected between the driest cases (e.g., Southern winter) to the high water vapor columns usually measured at the northern polar summer. For CO_2, which is only fit for spectra at order 167, a large variance (100%) was adopted to compensate for the small spectral impact of CO_2 lines.

Typical stochastic uncertainties resulting from OE for the derived water vapor column are of the order of 5%–10% (see Figure 1), however, the products presented herein are subject to other sources of systematic uncertainty. These include variable dust opacity and vertical distribution, and atmospheric state uncertainty. Each of these uncertainties impact the modeled line depths, and can account for a further 10% systematic uncertainty on retrievals. Other effects, such as underestimating multiple scattering from dust, have a much lower impact (2%–6%, e.g., Smith et al., 2021), except in the presence of global or regional dust events. Therefore, a maximum 20% absolute systematic uncertainty is conservatively prescribed to presented values, in excess of the random noise and in accordance with variation observed in pre-retrieval numerical experiments. Where overlapping observations exist, a weighted smoothing algorithm is employed that considers the relative uncertainty of the retrieved water vapor column as well as the spatial and temporal
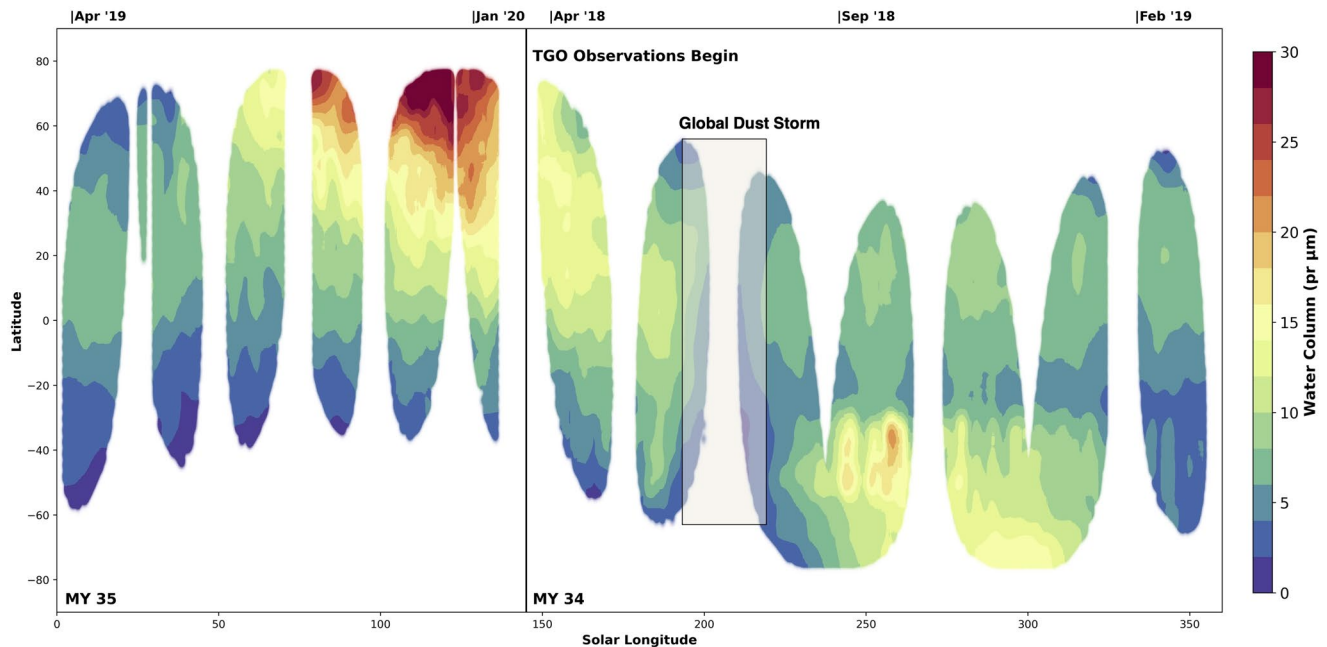
Figure 2. Observations of H$_2$O vapor column abundances, zonally averaged in longitude and scaled by 6 mbar, are presented for solar longitudes from the beginning of nominal science (March 2018) for almost an entire Martian Year (January 2020).

distances between the location of the observations. The smoothing kernel allows for the construction of maps of the Martian water cycle over different time scales, contrasting seasonal with diurnal, and across the planet's daylit hemisphere. This weighted average is similar to that used by Montabone et al. (2015), however, the parameters for weighting and temporal distance are unique to this work. When constructing zonal maps as a function of season (Figure 2) the weighting function's FWHM is about 4° in latitude, and 1.8° in *Ls*, or about three and a half sols. For maps of latitude and longitude (such as Figures 3 and 4), the error weighting function and area to consider has a FWHM of about 9°.

Retrievals are organized by latitude and longitude, within *Ls* = 325°–355°, in Figure 5, which are representative of the conditions represented in Figures 3 and 4. The local time coverage (Figure 5, top) shifts as TGO's orbit precesses while the SZA is roughly consistent (middle top) contrasting the columns in Figure 5. The signal and uncertainty are presented in the middle bottom and bottom rows, where the signal and uncertainty are colored to demonstrate a representative range of values.

4. Results

TGO's ability to map water vapor helps to extend our understanding of processes that control volatile transport in the lower atmosphere. Figure 2 presents the column abundance of water vapor as observed by NOMAD/LNO during MY 34 and 35, as a function of Solar Longitude and Latitude. Data shown here represent TGO's nominal science period from *Ls* = 140°, 26 March 2018 (black vertical line in Figure 2) to *Ls* = 135°, January 2020. These observations include only dayside observations whose solar zenith angle is less than 60°, where this constraint was chosen to exclude data without appreciable signal. Typical signal to noise ratios for those data with appreciable signal are around 20 (Figure 5). This data set represents the zonal average in a given *Ls* period, where the quality and number of observations in a location influences the smoothing kernel (described above).

The standard water vapor column abundance unit for Mars is pr-µm (precipitable microns), equivalent to 1 gram of water per square meter, which forms a 1 µm layer over this area as though one had precipitated the entire column onto the surface. These results are presented with (unscaled, Figure 3) and without (scaled, Figure 4) the effects of topography, which can be removed by normalizing the atmospheric surface pressure to 6 mbars (Smith, 2002). This process of scaling is a standard presentation of water vapor columns
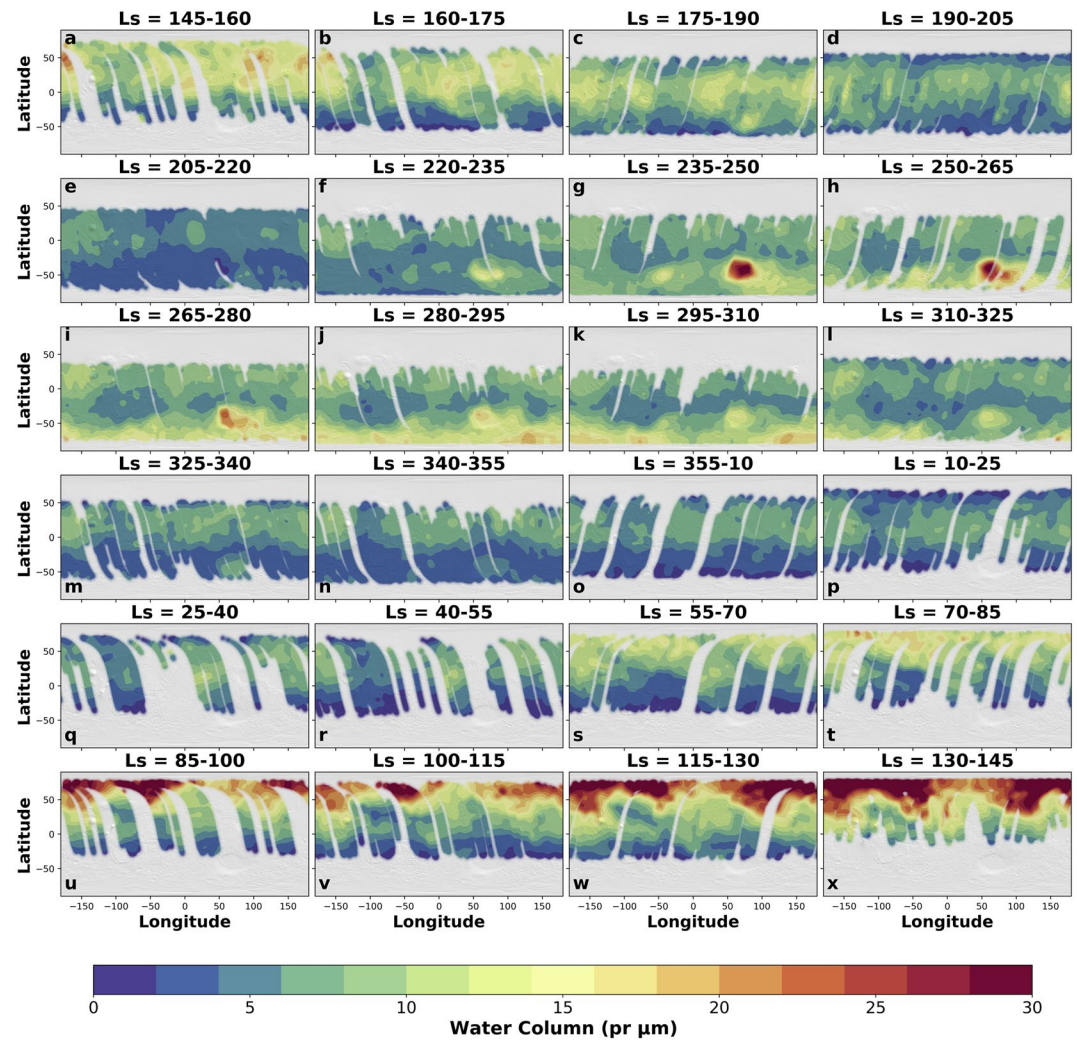
Figure 3. Observations of H_2O vapor column abundances presented on a topographic map of Mars (shown in gray). Each map is constructed as a weighted average, as discussed within Section 3 of the text, and sufficient observational overlap exists to separate the maps into *Ls* periods of 15°.

at Mars, but carries with it caveats in both cases. As such, the data is presented scaled and unscaled, since this scaling is predicated on the assumption that water vapor is well mixed with the ambient gases, which is not always the case, and both presentations have complementary merits. The pressure and CO_2 atmospheric densities, used as an a priori in the model retrieval as well, have been provided by the GEM global circulation model (Neary & Daerden, 2018). In this way, the effect of topographic features such as Hellas Basin and the Tharsis region can be minimized, as well as the overall slope from southern to northern latitudes. Figure 2 has been corrected for topography; however, the following sections will demonstrate the NOMAD results both with and without this correction.

Organizing the retrieved water maps without respect to geography allows for a direct examination of diurnal cycles in the total dayside water column, as the local time coverage is separable (Figure 5). While we do not find a strong dayside diurnal variation, this may not be entirely surprising given the vertical transport timescales for water interactions at the surface (on the order of hours), are unlikely to affect the entire vertical profile on those same timescales (Lewis, 2003). While previous work has shown that adsorption with regolith could impact the water vapor column by up to 10% (Böttger et al., 2005; Zent et al., 1993), the systematic uncertainty in the retrieved vertical column noted herein is in excess of these results and therefore LNO is not sensitive enough to determine the magnitude of any diurnal variation. LNO observations occur on the dayside of the planet, from the near dawn to near dusk local times, and observed variations appear
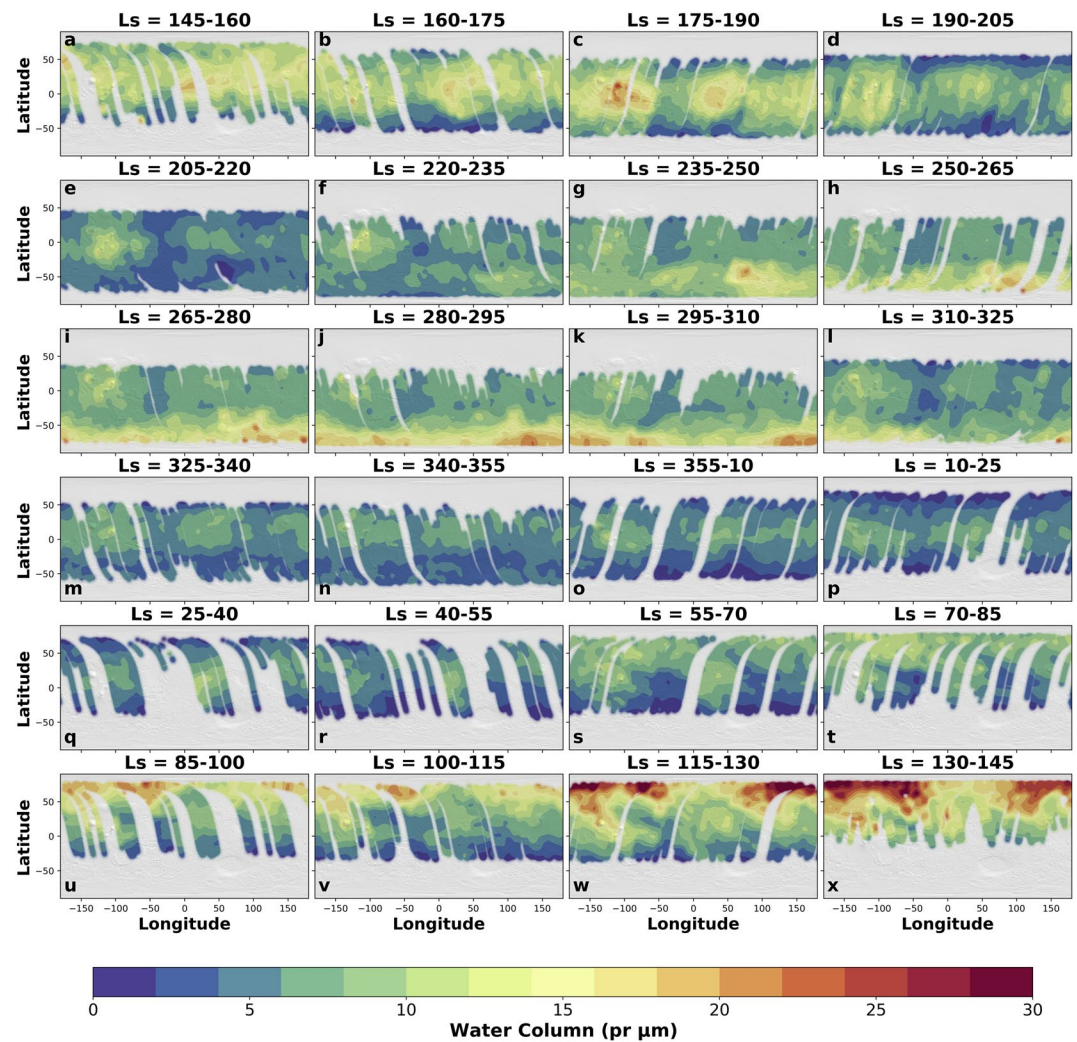
Figure 4. Same as Figure 3, however, the effects of topography have been removed by scaling them to the reference surface pressure of 6 mbar.

less than the systemic and random uncertainties noted herein. The effect of water ice cloud formation at 40 km or above is unlikely to have a dramatic effect in reducing the total observed vertical column, as the equivalent ice columns make a small fraction of the total water vapor column (Liuzzi et al., 2020). While cloud formation in the lowest layers of the atmosphere should lead significant changes in the water column, this study is unable to directly examine these effects due to a lack of simultaneous cloud observations and limitations due to the systematic uncertainty of these retrievals.

4.1. Overview

NOMAD column observations (Figure 2) show the pre-perihelion southward transport of water vapor from the northern polar region toward to the southern cap and subsequent deposition. Figure 2 presents pressure scaled column values, to represent a weighted longitudinal mean which is more agnostic to topographic variations. A global dust storm enveloped the planet starting at Mars Year 34, $Ls = 195°$, with a second smaller storm during the $Ls = 320°–340°$ time period (Aoki et al., 2019; Guzewich et al., 2019; Kass et al., 2019; Kleinböhl et al., 2020; Liuzzi et al., 2020; Sánchez-Lavega et al., 2019; Smith, 2019; Viúdez-Moreiras et al., 2019). With LNO observations beginning near $Ls = 150°$, water vapor has its largest equatorial latitudes peak of 15 pr-um. This equatorial value decreases to a minimum of 5 pr-um above the dust top, when the global dust event begins to dominate. During this time period, the systematic uncertainty is much larger (closer to
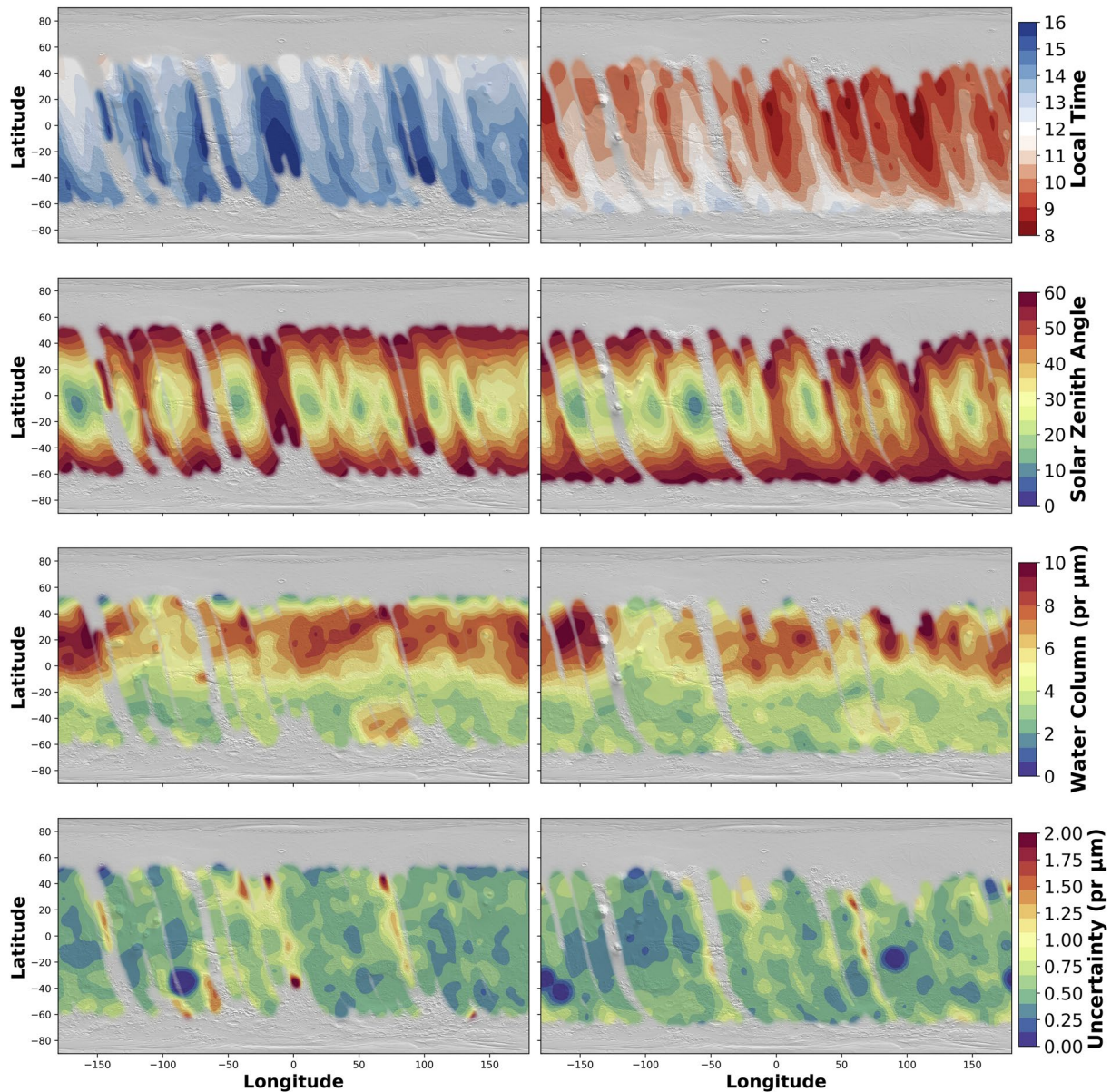
Figure 5. Observational characteristics of panels (m and n) from Figures 3 and 4, applying their same data smoothing. These panels represent typical observing conditions, where the left panels (m) represent panels (a, c, e, and g), and so on, and the right panels (n) represent panels (b, d, f, and h), and so on. Local times (top), solar zenith angles (middle top), retrieved water vapor column (middle bottom), and retrieval uncertainty (bottom) are shown for data that is representative of all of the other panels in Figures 3 and 4. The data and its uncertainty shown in the bottom two panels have not been scaled to remove topography.

50%), due to the abundance of dust in the lower atmosphere, so values between $Ls = 180°–220°$ should be interpreted as a lower limit. Previous observations of water vapor columns during global dust storms have indicated a decrease in overall column (Smith et al., 2009, 2018; Trokhimovskiy et al., 2015), however, due to constraints with aerosols NOMAD observation cannot directly test these results. Observations by the Curiosity Rover Mars Science Laboratory indicate an increase in the overall column locally during the peak of the global dust storm (Savijärvi et al., 2020). After the dissipation of the global dust storm, water vapor begins to appear above the haze top in the southern hemisphere, to a maximum of 20 pr-um, concentrated strongly at high southern latitudes near $Ls = 300°$. In the equatorial regions, there is minimal variation in water vapor with a uniform value of 6 pr-um from $Ls = 240°–350°$. Toward aphelion and northern summer, enhanced insolation of the northern cap leads to increased water vapor in the atmosphere. These columns

in the northern hemisphere peak near 30 pr-um, and are enhanced when accounting for the whole column (due to the northern hemispheric overall lowland topography), compared to the scaled values at 6 mbar.

Mars undergoes nonperiodic large-scale dust storm events, and the global dust storm of MY 34 peaked between $Ls = 195°$ and 220° (Guzewich et al., 2019; Kass et al., 2019; Sánchez-Lavega et al., 2019). While the presence of aerosols impacts the ability of NOMAD to retrieve the entire water column, the presence of strong lines in processed spectra and the results derived from these suggest water columns during this time period are reliable as lower limits. The rapid onset of the dust storm might suggest that water, being well mixed in the lower atmosphere, would be rapidly obscured at the beginning of the storm. However, recent work (Aoki et al., 2019; Chaffin et al., 2017; Fedorova et al., 2020; Heavens et al., 2018; Neary et al., 2019; Vandaele et al., 2019) has noted that global dust events may serve to elevate the hygropause, mixing water and dust in the lower atmosphere while lifting the former to altitudes (70 km) not seen outside of such events. The apparent reduction of water columns during this time, rather than their absence all together, indicates the ability to probe a nonnegligible fraction of the total water column (60% of the total assuming columns from previous MYs).

4.2. Geographic Variations

Across the first MY, TGO's orbit tracks precess with season, sweeping latitude and local time, therefore perceived diurnal changes, to first order, may actually be due to changes of water with season. Therefore, any geographic changes in water vapor observed by TGO must note these geophysical constraints during any subsequent analysis. Reducing the range of Ls considered in a single map to 15°, about an Earth month, TGO's coverage provides "snapshots" in time and with respect to the geographic location of the observations (Figures 3 and 4). In these maps, the presence of enhancements that are consistent between multiple time ranges indicate long lived features and can be distinguished from the effect of seasonal or diurnal change. Observations extend in Ls and latitude in round shapes, observed in Figure 2, and corresponds to those that begin centered over late local times, and sweep across the planet, ending over early local times. Therefore, in Figures 3a and 3c share similar local time coverage (afternoon) whereas Figures 3b and 3d that are centered around morning local times (see Figure 5). Features that persist between pairs of panels, for example, panels (g and h), represent a variety of local times, and therefore do not present strong evidence for diurnal changes in the dayside water column.

Water vapor in low to middle latitudes over the Tharsis and Arabia Terra regions (e.g., panels [c and d]) confirm previous measurements which also show enhancements of water vapor (e.g., Fouchet et al., 2007), which considered the result of the effects of atmospheric dynamics or potential release from the subsurface.

A set of dramatic geographic variations are present after the MY 34 global dust storm, near the Hellas basin region (latitudes 25°–55°S and longitudes 40°–100°E), where water vapor accumulates even when accounting for the depth of the Hellas (Figures 3 and 4, panels [f–i]). From $Ls = 235°–295°$, as Mars moves through southern summer, water vapor begins by appearing concentrated near the Hellas basin, and then expands southeastward. Geographic variations continue in the $Ls = 295°–325°$, the end of southern summer, where a significant enhancement of water vapor exists between 70° and 180° east longitude and 50°–70°S latitude. Observations from TES following the global dust storm of MY25 similarly show an enhancement in water vapor at these longitudes and extends poleward past the 70°S shown here (Pankine & Tamppari, 2019), demonstrating consistent climatology between these instruments. This effect is particularly pronounced in the $Ls = 280°–310°$ period (Figures 4j and 4k), where multiple regions in the southern polar latitudes have uneven distributions of water vapor, not associated with differences in topography. Similarly, $Ls = 130°–145°$ displays strong longitudinal variations at high northern latitudes (Figures 4w and 4x), particularly when accounting for topography.

After the solstice, and into southern hemispheric autumn ($Ls = 270°–330°$), Mars' global circulation of atmospheric volatiles becomes much more consistent with previous MYs (Figure 2). While the absolute abundance of atmospheric water vapor is not identical between other instruments and those presented here (see Section 5), the climatology is well reproduced and represents the previously observed trends of southern polar cap retreat, latitudinal transport, and deposition at the northern polar cap (Jakosky & Farmer, 1982). A second regional dust storm affected the planet during MY 34 between $Ls = 320°–340°$, which reflects similar

distributions of "reduced" water columns as the global dust storm previously in the year. During MY 35, as the northern polar cap begins to sublimate, NOMAD observes water column enhancements of 20 pr-um as early as $Ls = 85°$.

4.3. Absence of Strong Dayside Diurnal Variation

The orbit of TGO was designed to observe vertical profiles across the terminator twice per orbit as well as to map the dayside of the planet (Vandaele et al., 2018). The orbit precesses to observe most latitudes and sample corresponding regions, for example if SO tangent points begin in the northern hemisphere at high latitudes, they will move to the southern hemisphere over the course of 30° of Ls (two Earth months). In this way orientation of the nadir tracks sweep in roughly the same direction, and there is sufficient overlap to construct maps such as Figures 3 and 4, however, careful attention must be paid to the dominant driver of variations.

Figure 2 demonstrates that season is a dominant driver of variation with respect to latitude over long time scales, however, TGO's precessing orbit permits a closer look at the relative effect of season versus local time. Using a time period where water vapor exhibits little or gradual seasonal change, such as the equatorial region between $Ls = 325°$ and 25°, there is little variation in a single region, the Tharsis region for example. In particular, the zonal average of Figure 2 obscures the marked longitudinal variation that exists during this time period. Here, Figure 4m through Figure 4p demonstrate that the consistent water vapor columns observed in the Tharsis region are not strongly affected by diurnal changes. This can be inferred by noting that panels (m and o) have a mean local time near 14 and 15 hr, whereas panels (n and p) have a mean time near 10 and 9 hr, respectively.

5. Discussion

In order to compare the NOMAD observations to previous instruments and missions, important similarities and differences should be highlighted. NOMAD observations are overall lower in total water column than TES, where the distinction between the datasets appears multiplicative (30%) and not additive (such as ±5 pr-μm). The NOMAD Northern summer maximum water vapor columns are consistent with CRISM water vapor columns ∼30 pr-μm (Smith et al., 2018), whereas the TES observations (Smith, 2002) have peak columns of 70 pr-μm. It should be noted that TGO is unable to observe over either polar region, and when TES observations from MY 24–27 are averaged and compared to similar high northern latitudes from TGO, they compare more favorably (albeit still higher) with TES observations of 40–50 pr-μm compared to those reported here of just above 30 pr-μm. Therefore, attempts to use this data set for water cycle modeling should note this important geographical caveat, and instead comparisons between TGO, TES, CRISM, and so on and models should focus on their longitudinal and latitudinal coverage, the unique characteristic that TGO's orbit provides. TES and TGO observations are in agreement when describing the water climatology and seasonal variations with latitude, yet they observe different absolute columns. The difference in absolute column could be related to an actual interannual variability, true diurnal variation (TES samples at 2 p.m.), to differences in calibration and data processing techniques, and any combination of these factors. As noted previously, efforts to reconcile the TES, CRISM, and MAWD datasets has been attempted several times (Fedorova et al., 2004, 2010; Fouchet et al., 2007; Maltagliati, Titov, et al., 2011; Pankine et al., 2010; Tschimmel et al., 2008) without converging on a single interpretation of the peak column abundance for all instruments, this work does not attempt to definitively determine the water vapor abundance, instead these observations highlight the absolute differences, inherent in infrared observations (Maltagliati, Titov, et al., 2011), while noting climatological similarities.

These first water vapor retrievals with NOMAD LNO are useful to quantify the water vapor at differing local times than previous Sun-synchronous orbiting spacecraft. This provides constraints on the geographic and seasonal trends of water vapor, and ultimately establishes a relation with water ice clouds observations by NOMAD SO (Liuzzi et al., 2020), IUVS global maps of Martian clouds and dust (Connour et al., 2020; Stevens et al., 2017), MRO daily cloud maps (Malin & Cantor, 2019), and the MEx Imaging Camera data (Sánchez-Lavega et al., 2018).

6. Conclusions

TGO/NOMAD's water vapor mapping capabilities contributes to our understanding of processes that control transport of volatiles in the lower atmosphere. The NOMAD observations presented here span almost a full MY, and were conducted in multiple geometries and wavelength regions, with LNO observations sampling a wide variety of geophysical conditions. Water vapor absorption is a dominant feature in the three orders selected for these nadir observations, and were retrieved in suitable dayside columns with a state-of-the-art radiative transfer suite (PSG). While aerosols, such as lofted dust and water ice clouds, are not reliably extracted along the LNO line of sight, the modeled impact of their presence serves to set the lower limit on retrieved quantities. Combining retrievals with a weighted smoothing algorithm provides maps with respect to season and geographical coverage, including selection of data based on local time and solar zenith angle.

NOMAD observations confirm the overall character of the water vapor climatology observed by previous spacecraft, such as the northern hemispheric summer southward transport of water vapor from the northern polar region toward to the southern cap. TGO's orbital geometry and short period permits rapid geographic mapping, highlighting geographic variations observed after the global dust storm, near the Hellas basin region, even when accounting for topography. Geographic variations in the southern hemisphere continue in $Ls = 295°$–$325°$, the end of southern summer, where a significant enhancement of water vapor exists between 70° and 180° east longitude. These geographic variations, such as the abundance of water vapor during $Ls = 145°$–$175°$, may have a directly observable consequence in the Martian atmosphere, for example, on cloud formation or observations of ozone. Using geographic maps with slight seasonal change and disparate local times, these retrievals suggest there is insufficient evidence to imply diurnal changes. This confirms that, on the global scale, any surface exchange occurs in the lowest layer of the atmosphere, but that it is not the dominant source of variation of total water column.

The Martian water cycle has been studied with numerous spacecraft and Earth based observatories, providing an opportunity to compare and contrast differences. There exists some discrepancy in total column abundances, not readily explained, but potentially associated with the differences in remote sensing wavelength region or assumptions inherent in varying retrieval techniques. While NOMAD retrievals are consistent in peak values with CRISM, mid/equatorial latitude retrievals trend higher in the latter than the former. The TES retrievals show similar seasonal variability to the presented NOMAD columns, yet with different peak values.

Continued observation of Mars throughout the next Mars Year will complete TGO's initial survey of the Martian water cycle. With additional years of data, these maps will enable the study of interannual variability and constrain global transport of water vapor in the lower atmosphere.

Data Availability Statement

The raw and calibrated datasets used herein can be accessed on the ESA's Planetary Data Archive (http://archives.esac.esa.int/psa/#!Table%20View/NOMAD=instrument), and the retrieved parameters used herein from Orders 167, 168, and 169 are publicly available on Zenodo (https://doi.org/10.5281/zenodo.5510605).

References

Aoki, S., Vandaele, A. C., Daerden, F., Villanueva, G. L., Liuzzi, G., Thomas, I. R., et al. (2019). Water vapor vertical profiles on Mars in dust storms observed by TGO/NOMAD. *Journal of Geophysical Research: Planets*, *124*(12), 3482–3497. https://doi.org/10.1029/2019JE006109

Barth, C. A., Hord, C. W., Stewart, A. I., Lane, A. L., Dick, M. L., & Anderson, G. P. (1973). Mariner 9 ultraviolet spectrometer experiment: Seasonal variation of ozone on Mars. *Science*, *179*(4075), 795–796. https://doi.org/10.1126/science.179.4075.795

Bertaux, J.-L., Korablev, O., Perrier, S., Quémerais, E., Montmessin, F., Leblanc, F., et al. (2006). SPICAM on Mars Express: Observing modes and overview of UV spectrometer data and scientific results. *Journal of Geophysical Research*, *111*(E10). https://doi.org/10.1029/2006JE002690

Bibring, J.-P., Langevin, Y., Mustard, J. F., Poulet, F., Arvidson, R., Gendrin, A., et al. (2006). Global mineralogical and aqueous Mars history derived from OMEGA/mars express data. *Science*, *312*(5772), 400–404. https://doi.org/10.1126/science.1122659

Böttger, H. M., Lewis, S. R., Read, P. L., & Forget, F. (2005). The effects of the Martian regolith on GCM water cycle simulations. *Icarus*, *177*(1), 174–189. https://doi.org/10.1016/j.icarus.2005.02.024

Boynton, W. V. (2002). Distribution of hydrogen in the near surface of Mars: Evidence for subsurface ice deposits. *Science*, *297*(5578), 81–85. https://doi.org/10.1126/science.1073722

Chaffin, M. S., Deighan, J., Schneider, N. M., & Stewart, A. I. F. (2017). Elevated atmospheric escape of atomic hydrogen from Mars induced by high-altitude water. *Nature Geoscience*, *10*(3), 174–178. https://doi.org/10.1038/ngeo2887

Christensen, P. R., Bandfield, J. L., Hamilton, V. E., Ruff, S. W., Kieffer, H. H., Titus, T. N., et al. (2001). Mars global surveyor thermal emission spectrometer experiment: Investigation description and surface science results. *Journal of Geophysical Research*, *106*, 23823–23871. https://doi.org/10.1029/2000JE001370

Clancy, R. T., Montmessin, F., Benson, J., Daerden, F., Colaprete, A., & Wolff, M. J. (2017). Mars clouds. In F. Forget, M. D. Smith, R. T. Clancy, R. W. Zurek, & R. M. Haberle (Eds.), *The atmosphere and climate of Mars* (pp. 76–105). Cambridge University Press. https://doi.org/10.1017/9781139060172.005

Connour, K., Schneider, N. M., Milby, Z., Forget, F., Alhosani, M., Spiga, A., et al. (2020). Mars's twilight cloud band: A new cloud feature seen during the Mars Year 34 global dust storm. *Geophysical Research Letters*, *47*(1), e2019GL084997. https://doi.org/10.1029/2019GL084997

Fedorova, A. A., Montmessin, F., Korablev, O., Luginin, M., Trokhimovskiy, A., Belyaev, D. A., et al. (2020). Stormy water on Mars: The distribution and saturation of atmospheric water during the dusty season. *Science*, *367*(6475), 297–300. https://doi.org/10.1126/science.aay9522

Fedorova, A. A., Rodin, A. V., & Baklanova, I. V. (2004). MAWD observations revisited: Seasonal behavior of water vapor in the Martian atmosphere. *Icarus*, *171*(1), 54–67. https://doi.org/10.1016/j.icarus.2004.04.017

Fedorova, A. A., Trokhimovsky, S., Korablev, O., & Montmessin, F. (2010). Viking observation of water vapor on Mars: Revision from up-to-date spectroscopy and atmospheric models. *Icarus*, *208*(1), 156–164. https://doi.org/10.1016/j.icarus.2010.01.018

Formisano, V., Angrilli, F., Arnold, G., Atreya, S., Bianchini, G., Biondi, D., et al. (2005). The planetary Fourier spectrometer (PFS) onboard the European Mars Express mission. *Planetary and Space Science*, *53*(10), 963–974. https://doi.org/10.1016/j.pss.2004.12.006

Fouchet, T., Lellouch, E., Ignatiev, N. I., Forget, F., Titov, D. V., Tschimmel, M., et al. (2007). Martian water vapor: Mars Express PFS/LW observations. *Icarus*, *190*(1), 32–49. https://doi.org/10.1016/j.icarus.2007.03.003

Griffiths, P. R., & Haseth, J. A. D. (2007). *Fourier transform infrared spectrometry*. John Wiley & Sons.

Guzewich, S. D., Lemmon, M., Smith, C. L., Martínez, G., de Vicente-Retortillo, Á, Newman, C. E., et al. (2019). Mars science laboratory observations of the 2018/Mars Year 34 global dust storm. *Geophysical Research Letters*, *46*(1), 71–79. https://doi.org/10.1029/2018GL080839

Hase, F., Wallace, L., McLeod, S. D., Harrison, J. J., Bernath, P. F. (2010). The ACE-FTS atlas of the infrared solar spectrum. *Journal of Quantitative Spectroscopy and Radiative Transfer*, *111*(4), 521–528. https://doi.org/10.1016/j.jqsrt.2009.10.020

Heavens, N. G., Kleinböhl, A., Chaffin, M. S., Halekas, J. S., Kass, D. M., Hayne, P. O., et al. (2018). Hydrogen escape from Mars enhanced by deep convection in dust storms. *Nature Astronomy*, *2*(2), 126–132. https://doi.org/10.1038/s41550-017-0353-4

Jakosky, B. M., & Farmer, C. B. (1982). The seasonal and global behavior of water vapor in the Mars atmosphere: Complete global results of the Viking Atmospheric Water Detector Experiment. *Journal of Geophysical Research: Solid Earth*, *87*(B4), 2999–3019. https://doi.org/10.1029/JB087iB04p02999

Kahre, M. A., Murphy, J. R., Newman, C. E., Wilson, R. J., Cantor, B. A., Lemmon, M. T., & Wolff, M. J. (2017). The Mars dust cycle. In F. Forget, M. D. Smith, R. T. Clancy, R. W. Zurek, & R. M. Haberle (Eds.), *The atmosphere and climate of Mars* (pp. 295–337). Cambridge University Press. https://doi.org/10.1017/9781139060172.010

Kass, D. M., Schofield, J. T., Kleinböhl, A., McCleese, D. J., Heavens, N. G., Shirley, J. H., & Steele, L. J. (2019). Mars Climate Sounder observation of Mars' 2018 global dust storm. *Geophysical Research Letters*, *47*(23), e2019GL083931. https://doi.org/10.1029/2019GL083931

Kieffer, H. H., Chase, S. C., Martin, T. Z., Miner, E. D., & Palluconi, F. D. (1976). Martian north pole summer temperatures: Dirty water ice. *Science*, *194*(4271), 1341–1344. https://doi.org/10.1126/science.194.4271.1341

Kleinböhl, A., Spiga, A., Kass, D. M., Shirley, J. H., Millour, E., Montabone, L., & Forget, F. (2020). Diurnal variations of dust during the 2018 global dust storm observed by the Mars Climate Sounder. *Journal of Geophysical Research: Planets*, *125*(1), e2019JE006115. https://doi.org/10.1029/2019JE006115

Langevin, Y., Bibring, J.-P., Montmessin, F., Forget, F., Vincendon, M., Douté, S., et al. (2007). Observations of the south seasonal cap of Mars during recession in 2004–2006 by the OMEGA visible/near-infrared imaging spectrometer on board Mars Express. *Journal of Geophysical Research*, *112*(E8). https://doi.org/10.1029/2006JE002841

Lewis, S. R. (2003). Modelling the Martian atmosphere. *Astronomy and Geophysics*, *44*(4), 46–414. https://doi.org/10.1046/j.1468-4004.2003.44406.x

Liuzzi, G., Masiello, G., Serio, C., Venafra, S., & Camy-Peyret, C. (2016). Physical inversion of the full IASI spectra: Assessment of atmospheric parameters retrievals, consistency of spectroscopy and forward modelling. *Journal of Quantitative Spectroscopy and Radiative Transfer*, *182*, 128–157. https://doi.org/10.1016/j.jqsrt.2016.05.022

Liuzzi, G., Villanueva, G. L., Crismani, M. M. J., Smith, M. D., Mumma, M. J., Daerden, F., et al. (2020). Strong variability of Martian water ice clouds during dust storms revealed from ExoMars Trace Gas Orbiter/NOMAD. *Journal of Geophysical Research: Planets*, *125*(4), e2019JE006250. https://doi.org/10.1029/2019JE006250

Liuzzi, G., Villanueva, G. L., Mumma, M. J., Smith, M. D., Daerden, F., Ristic, B., et al. (2019). Methane on Mars: New insights into the sensitivity of CH_4 with the NOMAD/ExoMars spectrometer through its first in-flight calibration. *Icarus*, *321*, 671–690. https://doi.org/10.1016/j.icarus.2018.09.021

Malin, M. C., & B. A. Cantor,. (2019). *MRO MARCI Weather Report for the week of 26 August 2019–27 August 2019* (Malin Space Science Systems Captioned Image Release, MSSS-593). Retrieved from http://www.msss.com/msss_images/2019/09/04/

Maltagliati, L., Montmessin, F., Fedorova, A., Korablev, O., Forget, F., Bertaux, J.-L. (2011). Evidence of water vapor in excess of saturation in the atmosphere of Mars *Science 333*(6051), 1868–1871. https://doi.org/10.1126/science.1207957

Maltagliati, L., Titov, D. V., Encrenaz, T., Melchiorri, R., Forget, F., Keller, H. U., & Bibring, J.-P. (2011). Annual survey of water vapor behavior from the OMEGA mapping spectrometer onboard Mars Express. *Icarus*, *213*(2), 480–495. https://doi.org/10.1016/j.icarus.2011.03.030

Millour, E., Forget, F., Spiga, A., & Navarro, T. (2015). *The Mars Climate Database (MCD version 5.2)*. (Vol. 10). European Planetary Science Congress.

Montabone, L., Forget, F., Millour, E., Wilson, R. J., Lewis, S. R., Cantor, B., et al. (2015). Eight-year climatology of dust optical depth on Mars. *Icarus*, *251*, 65–95. https://doi.org/10.1016/j.icarus.2014.12.034

Montmessin, F., Smith, M., Langevin, Y., Mellon, M., & Fedorova, A. (2017). The water cycle. In *The atmosphere and climate of Mars*. Cambridge University Press.

Murchie, S., Arvidson, R., Bedini, P., Beisser, K., Bibring, J.-P., Bishop, J., et al. (2007). Compact reconnaissance imaging spectrometer for Mars (CRISM) on Mars Reconnaissance Orbiter (MRO). *Journal of Geophysical Research: Planets*, *112*(E5). https://doi.org/10.1029/2006JE002682

Neary, L., & Daerden, F. (2018). The GEM-Mars general circulation model for Mars: Description and evaluation. *Icarus*, *300*, 458–476. https://doi.org/10.1016/j.icarus.2017.09.028

Neary, L., Daerden, F., Aoki, S., Whiteway, J., Clancy, R. T., Smith, M., et al. (2019). Explanation for the increase in high altitude water on Mars observed by NOMAD during the 2018 global dust storm. *Geophysical Research Letters*, *47*(7), e2019GL084354. https://doi.org/10.1029/2019GL084354

Neefs, E., Vandaele, A. C., Drummond, R., Thomas, I. R., Berkenbosch, S., Clairquin, R., et al. (2015). NOMAD spectrometer on the ExoMars Trace Gas Orbiter mission: Part 1—Design, manufacturing and testing of the infrared channels. *Applied Optics*, *54*(28), 8494–8520. https://doi.org/10.1364/AO.54.008494

Pankine, A. A., & Tamppari, L. K. (2019). MGS TES observations of the water vapor in the Martian southern polar atmosphere during spring and summer. *Icarus*, *331*, 26–48. https://doi.org/10.1016/j.icarus.2019.05.010

Pankine, A. A., Tamppari, L. K., & Smith, M. D. (2010). MGS TES observations of the water vapor above the seasonal and perennial ice caps during northern spring and summer. *Icarus*, *210*(1), 58–71. https://doi.org/10.1016/j.icarus.2010.06.043

Patel, M. R., Antoine, P., Mason, J., Leese, M., Hathi, B., Stevens, A. H., et al. (2017). NOMAD spectrometer on the ExoMars Trace Gas Orbiter mission: Part 2—Design, manufacturing, and testing of the ultraviolet and visible channel. *Applied Optics*, *56*(10), 2771–2782. https://doi.org/10.1364/AO.56.002771

Rodgers, C. D. (2000). *Inverse methods for atmospheric sounding: Theory and practice*. World Scientific.

Sánchez-Lavega, A., Chen-Chen, H., Ordoñez-Etxeberria, I., Hueso, R., del Río-Gaztelurrutia, T., Garro, A., et al. (2018). Limb clouds and dust on Mars from images obtained by the Visual Monitoring Camera (VMC) onboard Mars Express. *Icarus*, *299*, 194–205. https://doi.org/10.1016/j.icarus.2017.07.026

Sánchez-Lavega, A., del Río-Gaztelurrutia, T., Hernández-Bernal, J., & Delcroix, M. (2019). The onset and growth of the 2018 Martian global dust storm. *Geophysical Research Letters*, *46*(11), 6101–6108. https://doi.org/10.1029/2019GL083207

Savijärvi, H., Martinez, G., Harri, A.-M., & Paton, M. (2020). Curiosity observations and column model integrations for a Martian global dust event. *Icarus*, *337*, 113515. https://doi.org/10.1016/j.icarus.2019.113515

Smith, M. D. (2002). The annual cycle of water vapor on Mars as observed by the Thermal Emission Spectrometer. *Journal of Geophysical Research*, *107*(E11), 25-1–25-19. https://doi.org/10.1029/2001JE001522

Smith, M. D. (2004). Interannual variability in TES atmospheric observations of Mars during 1999–2003. *Icarus*, *167*(1), 148–165. https://doi.org/10.1016/j.icarus.2003.09.010

Smith, M. D. (2019). THEMIS observations of the 2018 Mars global dust storm. *Journal of Geophysical Research: Planets*, *124*(11), 2929–2944. https://doi.org/10.1029/2019JE006107

Smith, M. D., Daerden, F., Neary, L., & Khayat, A. (2018). The climatology of carbon monoxide and water vapor on Mars as observed by CRISM and modeled by the GEM-Mars general circulation model. *Icarus*, *301*, 117–131. https://doi.org/10.1016/j.icarus.2017.09.027

Smith, M. D., Daerden, F., Neary, L., Khayat, A. S. J., Holmes, J. A., Patel, M. R., et al. (2021). The climatology of carbon monoxide on Mars as observed by NOMAD nadir-geometry observations. *Icarus*, *362*, 114404. https://doi.org/10.1016/j.icarus.2021.114404

Smith, M. D., Wolff, M. J., Clancy, R. T., Kleinböhl, A., & Murchie, S. L. (2013). Vertical distribution of dust and water ice aerosols from CRISM limb-geometry observations. *Journal of Geophysical Research: Planets*, *118*(2), 321–334. https://doi.org/10.1002/jgre.20047

Smith, M. D., Wolff, M. J., Clancy, R. T., & Murchie, S. L. (2009). Compact Reconnaissance Imaging Spectrometer observations of water vapor and carbon monoxide. *Journal of Geophysical Research*, *114*. https://doi.org/10.1029/2008JE003288

Spinrad, H., Münch, G., & Kaplan, L. D. (1963). Letter to the editor: The detection of water vapor on Mars. *The Astrophysical Journal*, *137*, 1319. https://doi.org/10.1086/147613

Stevens, M. H., Siskind, D. E., Evans, J. S., Jain, S. K., Schneider, N. M., Deighan, J., et al. (2017). Martian mesospheric cloud observations by IUVS on MAVEN: Thermal tides coupled to the upper atmosphere. *Geophysical Research Letters*, *44*(10), 4709–4715. https://doi.org/10.1002/2017GL072717

Thomas, I. R., Vandaele, A. C., Robert, S., Neefs, E., Drummond, R., Daerden, F., et al. (2016). Optical and radiometric models of the NOMAD instrument part II: The infrared channels—SO and LNO. *Optics Express*, *24*(4), 3790–3805. https://doi.org/10.1364/OE.24.003790

Trokhimovskiy, A., Fedorova, A., Korablev, O., Montmessin, F., Bertaux, J.-L., Rodin, A., & Smith, M. D. (2015). Mars' water vapor mapping by the SPICAM IR spectrometer: Five Martian Years of observations. *Icarus*, *251*, 50–64. https://doi.org/10.1016/j.icarus.2014.10.007

Tschimmel, M., Ignatiev, N. I., Titov, D. V., Lellouch, E., Fouchet, T., Giuranna, M., & Formisano, V. (2008). Investigation of water vapor on Mars with PFS/SW of Mars Express. *Icarus*, *195*(2), 557–575. https://doi.org/10.1016/j.icarus.2008.01.018

Vandaele, A. C., Korablev, O., Daerden, F., Aoki, S., Thomas, I. R., Altieri, F., et al. (2019). Martian dust storm impact on atmospheric H_2O and D/H observed by ExoMars Trace Gas Orbiter. *Nature*, *568*(7753), 521–525. https://doi.org/10.1038/s41586-019-1097-3

Vandaele, A. C., Lopez-Moreno, J.-J., Patel, M. R., Bellucci, G., Daerden, F., Ristic, B., et al. (2018). NOMAD, an integrated suite of three spectrometers for the ExoMars Trace Gas Mission: Technical description, science objectives and expected performance. *Space Science Reviews*, *214*(5), 80. https://doi.org/10.1007/s11214-018-0517-2

Vandaele, A. C., Mahieux, A., Robert, S., Berkenbosch, S., Clairquin, R., Drummond, R., et al. (2013). Improved calibration of SOIR/Venus Express spectra. *Optics Express*, *21*(18), 21148–21161. https://doi.org/10.1364/OE.21.021148

Villanueva, G. L., Smith, M. D., Protopapa, S., Faggi, S., & Mandell, A. M. (2018). Planetary Spectrum Generator: An accurate online radiative transfer suite for atmospheres, comets, small bodies and exoplanets. *Journal of Quantitative Spectroscopy and Radiative Transfer*, *217*, 86–104. https://doi.org/10.1016/j.jqsrt.2018.05.023

Viúdez-Moreiras, D., Newman, C. E., dela Torre, M., Martínez, G., Guzewich, S., Lemmon, M., et al. (2019). Effects of the MY34/2018 global dust storm as measured by MSL REMS in gale crater. *Journal of Geophysical Research: Planets*, *124*(7), 1899–1912. https://doi.org/10.1029/2019JE005985

Zent, A. P., Haberle, R. M., Houben, H. C., & Jakosky, B. M. (1993). A coupled subsurface-boundary layer model of water on Mars. *Journal of Geophysical Research*, *98*(E2), 3319–3337. https://doi.org/10.1029/92JE02805